Electron-phonon coupling and thermal transport in the thermoelectric compound Mo_{3}Sb_{7−x}Te_{x}

Dipanshu Bansal, Chen W. Li, Ayman H. Said, Douglas L. Abernathy, Jiaqiang Yan, and Olivier Delaire

Electron-phonon coupling and thermal transport in the thermoelectric compound $\mathrm{Mo_3Sb_{7-x}Te_x}$

Dipanshu Bansal,[1] Chen W. Li,[1] Ayman H. Said,[2] Douglas L. Abernathy,[3] Jiaqiang Yan,[1,4] and Olivier Delaire[1*]

[1]*Materials Science and Technology Division, Oak Ridge National Laboratory, Oak Ridge, Tennessee 37831, USA*
[2]*Advanced Photon Source, Argonne National Laboratory, Argonne, Illinois 60439, USA*
[3]*Quantum Condensed Matter Division, Oak Ridge National Laboratory, Oak Ridge, Tennessee 37831, USA*
[4]*Department of Materials Science and Engineering,
University of Tennessee, Knoxville, Tennessee 37996, USA*
(Dated: November 13, 2015)

Phonon properties of $\mathrm{Mo_3Sb_{7-x}Te_x}$ ($x = 0, 1.5, 1.7$), a potential high-temperature thermoelectric material, have been studied with inelastic neutron and x-ray scattering, and with first-principles simulations. The substitution of Te for Sb leads to pronounced changes in the electronic structure, local bonding, phonon density of states (DOS), dispersions, and phonon lifetimes. Alloying with tellurium shifts the Fermi level upward, near the top of the valence band, resulting in a strong suppression of electron-phonon screening, and a large overall stiffening of interatomic force-constants. The suppression in electron-phonon coupling concomitantly increases group velocities and suppresses phonon scattering rates, surpassing the effects of alloy-disorder scattering, and resulting in a surprising increased lattice thermal conductivity in the alloy. We also identify that the local bonding environment changes non-uniformly around different atoms, leading to variable perturbation strengths for different optical phonon branches. Changes in phonon group velocities and phonon scattering rates are quantified, highlighting the large effect of electron-phonon coupling in this compound.

PACS numbers: 63.20.D-, 63.20.kd, 66.30.Xj

I. INTRODUCTION

Thermoelectric materials convert temperature gradients into electrical potentials, and are of widespread interest for their applications in solid-state power generation or refrigeration [1–6]. Good thermoelectric conversion efficiency is dependent on achieving large values of Seebeck coefficient, S, high electrical conductivity, σ, and at the same time a low thermal conductivity, κ. The total thermal conductivity is the sum of an electrical contribution from charge carriers, κ_{el}, and a lattice component κ_{L} due to phonon propagation. In order to maximize the thermoelectric figure-of-merit, $ZT = S^2\sigma T/(\kappa_{\mathrm{el}} + \kappa_{\mathrm{L}})$, much effort is focused toward suppressing phonon propagation to minimize κ_{L} [1–4, 7–12].

$\mathrm{Mo_3Sb_7}$ is an over-doped p-type metallic compound and in order to improve its thermoelectric performance, one needs to dope extra electrons to reduce its carrier concentration [13, 14]. Adding electrons shifts the Fermi level toward the top of the valence band and increases the power factor (defined by product of square of Seebeck coefficient and electrical conductivity, $S^2\sigma$). Prior studies investigating electrical transport in $\mathrm{Mo_3Sb_{7-x}Te_x}$ show a definite increase in power factor up to x = 1.8 [13–19]. Such alloying would normally be expected to reduce κ_{L} through impurity scattering [20, 21]. However, the introduction of Te in $\mathrm{Mo_3Sb_7}$ leads instead to a surprising increase in κ_{L} [13, 16, 17, 19]. This effect was attributed to a suppression in electron-phonon coupling as the hole concentration is reduced with Te doping [13, 22].

$\mathrm{Mo_3Sb_7}$ has also attracted strong interest because of its unusual magnetic and superconducting properties [23–31]. $\mathrm{Mo_3Sb_7}$ undergoes a magnetic and structural phase transition at $T \simeq 53\,\mathrm{K}$, from a high-temperature cubic phase ($Im\bar{3}m$) to a low-temperature tetragonal phase ($I4/mmm$), corresponding to a contraction of Mo-Mo nearest-neighbor bonds along the $c-$axis, and the formation of singlet dimers. However, the distortion from the cubic structure is slight, with the a/c ratio reaching 1.002 at 11 K according to single-crystal x-ray diffraction [32]. Doping with Te strongly suppresses the structural phase transition temperature, and no phase transition is observed for Te concentrations exceeding 0.36% [32].

Prior inelastic neutron scattering (INS) investigations at low temperature ($T \leq 300K$) have revealed a possible deviation from the quasi-harmonic (QH) approximation in the case of $\mathrm{Mo_3Sb_7}$, as opposed to a normal QH behavior in $\mathrm{Mo_3Sb_{5.4}Te_{1.6}}$ [22]. However, that study was limited to powder measurements of the phonon DOS at few temperatures. While Shi et al. [13] investigated the thermal transport properties at high temperatures using transport and calorimetry measurements, momentum-resolved spectroscopic information about the phonon dispersions is still lacking. Here, we provide a detailed analysis of the effect of electron-phonon coupling by combining measurements of the phonon dispersions and density of states with x-ray and neutron scattering, and density functional theory (DFT) simulations including alloying effects explicitly.

In the present study, we performed a comprehensive set of phonon measurements, complemented with first-principles simulations, which enable us to quantitatively assess the effect of Te alloying on the lattice dynamics

---

* bansald@ornl.gov; delaireoa@ornl.gov

and phonon transport in $Mo_3Sb_{7-x}Te_x$. We investigated the phonon DOS of powders with INS in $Mo_3Sb_{7-x}Te_x$ ($x = 0, 1.7$) for 12 temperatures over a wide range ($6 \leqslant T \leqslant 750\,\mathrm{K}$). In addition, we performed inelastic x-ray scattering (IXS) measurements of low-energy phonon dispersions on single crystals in $Mo_3Sb_{7-x}Te_x$ ($x = 0, 1.5$) at $T = 100, 300\,\mathrm{K}$. We also performed density functional calculations of phonons for both the parent compound and Te-doped supercells representing the alloy, and gained insights into changes in bonding. We combined our experiments and simulations to model the contributions of different phonon scattering mechanisms to κ_L, which we compare with the reported thermal conductivity data. Our results clearly show that the electron-phonon coupling strongly affects the lattice dynamics and thermal conductivity in Mo_3Sb_7, and is suppressed with Te alloying. Our analysis also points to an increase in phonon scattering owing to the coupled magnetic-structural fluctuations around $53\,\mathrm{K}$ in the undoped compound, although the magnetism does not appreciably alter the overall force-constants and phonon energies.

II. SAMPLE PREPARATION

Polycrystalline $Mo_3Sb_{7-x}Te_x$ ($x = 0, 1.7$) samples were synthesized by a solid-state reaction method. A homogeneous mixture (15 grams) of Mo (Alfa, 99.999%), Sb (Alfa, 99.9999%), and Te (Alfa, 99.9999%) powder was loaded into a quartz tube and sealed under approximately 1/3 atmosphere of argon gas. The Mo powder was first reduced in flowing Ar balanced with 4% H2 for overnight at $1273\,\mathrm{K}$. The sealed ampoules were heated to $993\,\mathrm{K}$ in 12 hours and kept at this temperature for three weeks. Room temperature x-ray powder diffraction measurements confirmed that both compositions had no impurity and were single-phase (cubic $Im\bar{3}m$). Furthermore, relative lattice parameter contraction in doped composition in comparison to undoped composition confirmed that the Te content is close to the nominal one. The superconducting transition temperature of $T_c = 2.30\,\mathrm{K}$ was confirmed for the parent compound by measuring magnetic susceptibility using a Quantum Design Magnetic Property Measurement System. No sign of superconductivity at $1.80\,\mathrm{K}$ was observed in the powder sample with nominal composition of $Mo_3Sb_{5.3}Te_{1.7}$.

Millimeter sized $Mo_3Sb_{7-x}Te_x$ ($x = 0, 1.5$) single crystals were grown with a self-flux method technique [27, 32]. The real composition of as-grown crystals was determined by elemental analysis performed with a Hitachi TM-3000 tabletop electron microscope equipped with a Bruker Quantax 70 energy dispersive x-ray system. Mo_3Sb_7 is the only line compound in Mo-Sb binary system, and our elemental analysis indicated no deviation from stoichiometry. The real composition of the Te-doped crystals was determined to be $Mo_3Sb_{5.48}Te_{1.52}$. Mo_3Sb_7 single crystals used in this study have been well

characterized, as previously reported [27]. Magnetic measurements confirmed that $Mo_3Sb_{5.48}Te_{1.52}$ single crystals do not superconduct above $1.8\,\mathrm{K}$.

III. INELASTIC SCATTERING EXPERIMENTS

A. Neutron Scattering

Inelastic neutron scattering measurements on $Mo_3Sb_{7-x}Te_x$ ($x = 0, 1.7$) powders were carried out using the ARCS time-of-flight chopper spectrometer at the Spallation Neutron Source (SNS) at Oak Ridge National Laboratory [33]. The powders (mass $\sim 10\,\mathrm{g}$) were encased in thin-walled aluminum cans. Measurements at low temperature ($5 \leq T \leq 300\,\mathrm{K}$) were performed with the sample container inside a closed-cycle helium refrigerator, with the sample chamber filled with a low pressure of helium. High-temperature ($300 \leq T \leq 750\,\mathrm{K}$) measurements used a low-background resistive furnace. All measurements used an oscillating radial collimator to minimize scattering from the sample environment. The empty aluminum can was measured in identical conditions at all temperatures. Two incident neutron energies $E_i = 30\,\mathrm{meV}$ and $55\,\mathrm{meV}$ were used at each temperature, to provide higher resolution data for low-energy optic modes, and to probe the full spectrum, respectively. The energy resolution (full width at half maximum) for incident energies $E_i = 30\,\mathrm{meV}$ and $55\,\mathrm{meV}$ are $\sim 1.3\,\mathrm{meV}$ and $\sim 2.2\,\mathrm{meV}$ at elastic line, respectively, which reduces to $\sim 0.4\,\mathrm{meV}$ and $\sim 1.2\,\mathrm{meV}$ at energy transfer of $30\,\mathrm{meV}$.

The data were normalized by the total incident flux, and corrected for detector efficiency. The transformation of data from instrument coordinates to the physical momentum transfer, Q, and energy transfer, E, was performed using the MANTID reduction software [34]. The scattering from the empty container was processed identically and subtracted from the sample measurements. The analysis of the phonon DOS was performed within the incoherent scattering approximation, and corrected for the effect of multiphonon scattering [35]. The data in the region of the elastic peak were removed, and a Debye-like quadratic energy dependence was used to extrapolate the DOS at low energy ($E < 2\,\mathrm{meV}$ for $E_i = 30\,\mathrm{meV}$ and $E < 4\,\mathrm{meV}$ for $E_i = 55\,\mathrm{meV}$).

The phonon spectra derived from INS measurements are skewed by the relative neutron scattering strengths of the elements present in the sample (neutron-weighting, NW). The partial phonon DOS of each element is weighted differently, according to the ratio of that element's scattering cross-section (σ) and mass (m). The neutron weighting factors for Mo, Sb, and Te are $\sigma_{Mo}/m_{Mo} = 0.0595$, $\sigma_{Sb}/m_{Sb} = 0.0320$, and $\sigma_{Te}/m_{Te} = 0.0339$, respectively (in units of barns/amu). Consequently, the total experimentally measured phonon DOS, $g(E)$, for $Mo_3Sb_{7-x}Te_x$ is over-weighted for the Mo vi-

brational contributions:

$$g_{NW}(E) = [3 \times \frac{\sigma_{Mo}}{m_{Mo}} g_{Mo}(E) + (7-x) \times \frac{\sigma_{Sb}}{m_{Sb}} g_{Sb}(E)$$
$$+ x \times \frac{\sigma_{Te}}{m_{Te}} g_{Te}(E)]/10 \,, \qquad (1)$$

where $g_{Mo}(E)$, $g_{Sb}(E)$, and $g_{Te}(E)$ are the partial densities of states of Mo, Sb, and Te. However, the resulting neutron-weighted phonon DOS can be directly compared against the simulated DOS to which the same neutron-weights are applied (see below). We note that in this study, we keep the overall and partial phonon DOS normalized to a unit integral.

B. X-ray Scattering

Phonon dispersion curves of $Mo_3Sb_{7-x}Te_x$ ($x = 0, 1.5$) were extracted from the high resolution inelastic x-ray scattering (IXS) measurements on small single-crystals, using beamline 30-ID-C (HERIX [36, 37]) at the Advanced Photon Source (APS). The highly monochromatic x-ray beam had an energy $E \simeq 23.7$ keV ($\lambda = 0.5226$ Å), with an energy resolution $\Delta E \sim 1.0$ meV (full width at half maximum), and was focused on the sample with a beam cross-section $\sim 35 \times 15\,\mu$m (horizontal×vertical). The convoluted energy resolution of monochromatic x-ray beam and analyzer crystal was $\Delta E \sim 1.5$ meV. The single crystals of Mo_3Sb_7 and $Mo_3Sb_{5.5}Te_{1.5}$ were approximately ~ 2 mm across with well defined facets. The measurements were performed in reflection geometry off (100) facets, with the crystals glued to Beryllium posts using varnish, and mounted in a closed-cycle helium refrigerator. A crystal used for IXS is shown in figure 1-a. Typical counting times were in the range of 40 to 120 s at each point in energy scans at constant $\boldsymbol{Q}$.

The orientation matrix was defined using (6,6,0) and (0,6,0) Bragg peaks, and checked with other peaks. The longitudinal and transverse acoustic dispersions along high symmetry directions were measured along $(0, 6+\xi, 0)$, $(0, 6, \xi)$, $(6+\xi, 6+\xi, 0)$, $(6-\xi, 6+\xi, 0)$, $(\xi, 6, -\xi)$, and $(\xi, 6-\xi, -\xi)$. The spectra were fitted with a damped-harmonic-oscillator scattering function [38], subsequently convoluted with the measured instrumental resolution function, $R * S(E)$:

$$S(E) = A \frac{\{\frac{1}{2} \pm \frac{1}{2} + n(|E|)\} \times \frac{1}{2}\Gamma_{LW}}{(E^2 - E_0^2)^2 + (\frac{1}{2}\Gamma_{LW})^2} + B \,, \qquad (2)$$

where B is the constant background, $n(E)$ is the temperature-dependent Bose-Einstein distribution at phonon energy transfer E, A is the amplitude, Γ_{LW} is full phonon linewidth at half maximum, and E_0 is the bare phonon energy in the absence of damping (the $+$ sign is for $E > 0$ and $-$ sign for $E < 0$). Typical IXS spectra and the corresponding fits are shown in figure 1.
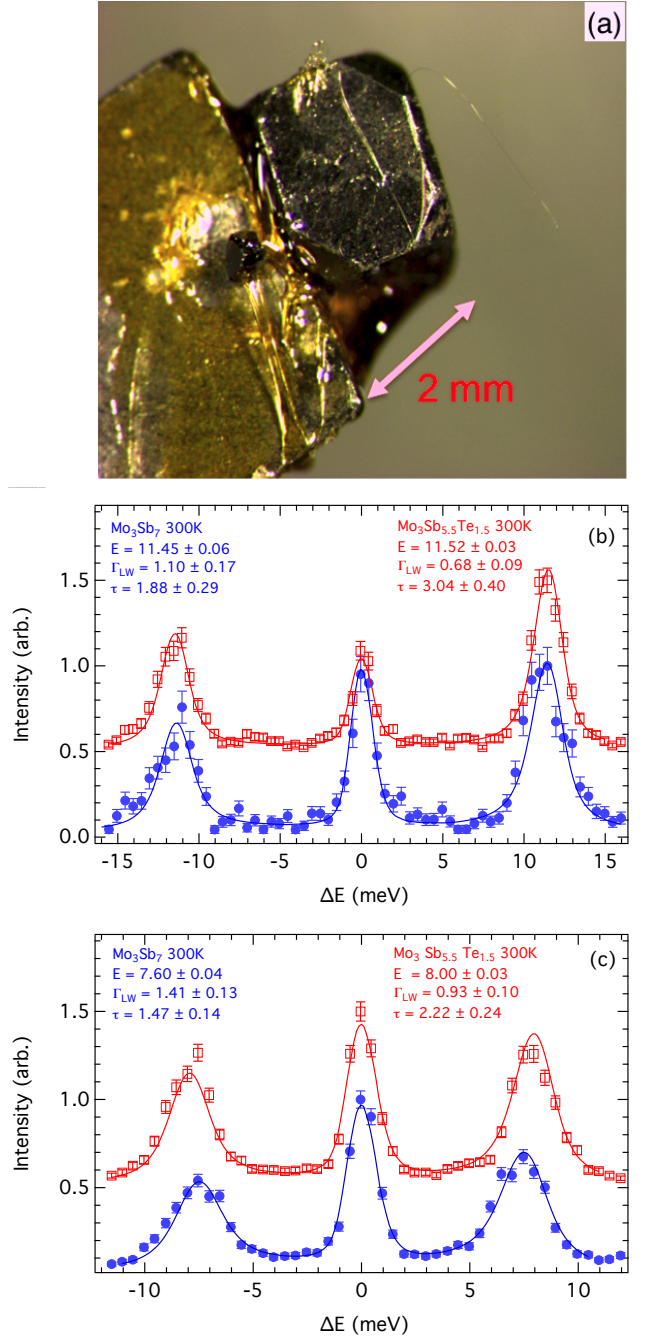

FIG. 1. (a) Mo_3Sb_7 single crystal glued on beryllium post using varnish. The main facet, about 2 mm across, corresponds to the (100) crystallographic plane. The very small crystal on the side of the beryllium mount was not used. (b) Constant-$\boldsymbol{Q}$ inelastic x-ray scattering spectra for longitudinal acoustic mode at $\boldsymbol{Q} = (0, 6.6, 0)$ for Mo_3Sb_7 (filled blue circles) and $Mo_3Sb_{5.5}Te_{1.5}$ (empty red squares) at 300 K. The lines are fits using a damped harmonic oscillator profile convoluted with the instrument resolution (see text). The values of E (in meV), Γ_{LW} (in meV), and τ (in picosecond) listed in inset are the fitted phonon energy, phonon linewidth (corrected for resolution), and phonon lifetime, respectively. Negative ΔE corresponds to phonon annihilation, and positive ΔE to phonon creation. (c) Same as (b) for $\boldsymbol{Q} = (0, 6.4, 0)$.

IV. DENSITY FUNCTIONAL THEORY SIMULATIONS

First-principles simulations were performed in the framework of density functional theory (DFT) as implemented in the Vienna Ab initio Simulation Package (VASP 5.3) [39–42]. A $4\times4\times4$ Monkhorst Pack electronic k-point mesh was used for all of our simulations, with a plane-wave cut-off energy of $500\,\text{eV}$. The projector-augmented-wave potentials explicitly included 14 valence electrons for Mo $(4s^24p^65s^14d^5)$, 5 for Sb $(5s^25p^3)$, and 6 for Te $(5s^25p^4)$. All our calculations used the generalized gradient approximation with PBE parametrization [43].

During the relaxation of the structure, the lattice parameters were kept fixed at the experimental value for the cubic phase at room temperature [16, 44], and atomic positions were optimized until forces on all atoms were smaller than $1\,\text{meV}\,\text{Å}^{-1}$. The calculations of phonon dispersions were performed in the harmonic approximation, using the finite displacement approach as implemented in Phonopy [45, 46], with the atomic forces in the distorted supercells obtained with VASP. In the case of Mo_3Sb_7, the phonon calculations used a $2 \times 2 \times 2$ supercell of the primitive cell, containing 160 atoms.

To describe the random alloy with $x = 1.5$, we built two cubic supercells (40 atoms), in which six Sb atoms were replaced with six Te atom to represent Mo:Sb:Te :: 3:5.5:1.5 composition as $\text{Mo}_{12}\text{Sb}_{22}\text{Te}_6$. The cubic unit cells of Mo_3Sb_7 and the two cells representing the alloy $\text{Mo}_3\text{Sb}_{5.5}\text{Te}_{1.5}$ are shown in figure 2. In the body-centered-cubic structure (BCC) of Mo_3Sb_7, the Mo, Sb(1), and Sb(2) atoms occupy crystallographic sites 12e, 12d, and 16f. Prior studies of $\text{Mo}_3\text{Sb}_{7-x}\text{Te}_x$ have shown, using neutron diffraction and ab initio computations of energetics, that Te substitution occurs preferentially at the 12d site as opposed to 16f [44]. Hence, in building the 40-atom supercells describing the alloy, we have replaced 6 Sb(1) atoms at site 12d with 6 Te atoms. There are multiple possible choices for placing six Te atoms on the Sb(1) sites. To limit the computational requirements, we chose two configurations (case 1 and case 2), illustrated in figure 2. To compute phonons for the alloy, $2 \times 2 \times 2$ supercells of the two alloy cells in each case (the two phonon supercells contained 320 atoms). To construct the force-constant matrix using the finite displacement approach, we computed 5, 26 and 36 independent atomic displacements for the undoped cell, case 1, and case 2, respectively. The atomic displacement amplitude was one hundredth of the lattice constant.

V. RESULTS AND DISCUSSION

A. Phonon Density of States

The neutron-weighted phonon DOS from INS are shown in figures 3 and 4 for Mo_3Sb_7 and $\text{Mo}_3\text{Sb}_{5.3}\text{Te}_{1.7}$, respectively, at the different temperatures measured and

for the two incident energies used. A clear softening of phonons (shift to lower frequencies) is observed over the full phonon DOS when increasing temperature, but with quite different magnitudes in the doped and undoped compounds. To analyze this softening, we have compared the mean phonon energy $\langle E \rangle$ with the expected softening upon thermal expansion within the quasi-harmonic (QH) approximation. We use an average thermodynamic Grüneisen parameter $\gamma = 3\alpha V K_T / C_v$, where α is coefficient of linear thermal expansion, V is the unit cell volume, K_T the iso-thermal bulk modulus, and C_v the heat capacity at constant volume (per unit cell). The iso-thermal bulk modulus was obtained from the phonon group velocities at $300\,\text{K}$ derived from our IXS measurements (table III), while C_v^{ph} was calculated from the phonon DOS measured at T=6 K, in the harmonic approximation, and magnetic and electronic contributions to the specific heat were added at low temperatures [26]. We obtain $\gamma = 1.25$ and 0.70 for Mo_3Sb_7 and $\text{Mo}_3\text{Sb}_{5.3}\text{Te}_{1.7}$, respectively. It can be observed from figure 5-b, that, while both materials deviate from the QH approximation for $T > 300\,\text{K}$, this deviation is more pronounced in the undoped system at low temperatures $T \leq 200K$. While $\text{Mo}_3\text{Sb}_{5.3}\text{Te}_{1.7}$ follows the QH behavior fairly well at low T, Mo_3Sb_7 displays an unusual temperature dependence and softens much faster, in agreement with the data reported by Candolfi *et al.* [22]. As we will show later, this pronounced softening in Mo_3Sb_7 is due to the electron-phonon coupling, which strongly influences phonon energies, lifetimes, and group velocities. We point out that the INS data on powders do not show much change across the $53\,\text{K}$ phase transition in Mo_3Sb_7. We could not detect any magnetic scattering intensity at low $|Q|$ (see figure 6). The NW phonon DOS curves also show little change between $40\,\text{K}$ and $65\,\text{K}$ (figure 3), indicating a relatively weak effect of magnetic correlations on the overall lattice dynamics (force-constants) in this system. However, the magnetic fluctuations and the distortions from pairing of Mo dimers are likely to lead to increased phonon scattering rates (increased linewidths), which would not be easily detectable in the phonon DOS. Our analysis of thermal transport based on phonon group velocities reveal this effect more clearly (see below).

Figure 7 illustrates the effect of Te alloying. A significant stiffening $\Delta E \sim 1.0\,\text{meV}$ is observed upon introduction of Te, and results from a combination of decrease in lattice parameter upon Te doping and of reduction in carrier concentration (from $\sim 10^{22}\ cm^{-3}$ in Mo_3Sb_7 to $\sim 10^{21}\ cm^{-3}$ in $\text{Mo}_3\text{Sb}_{5.3}\text{Te}_{1.7}$ [13]). Importantly, the contraction in lattice parameter with Te doping ($\Delta a/a \sim 0.1\%$ [44]) only accounts for 0.35% of the observed phonon DOS stiffening. Thus, additional mechanisms such as the change in bonding and suppression in electron-phonon coupling could explain the large observed stiffening. The stiffening with Te doping occurs at all temperatures and remains fairly constant with temperature (see figure 5(f, g, h)).

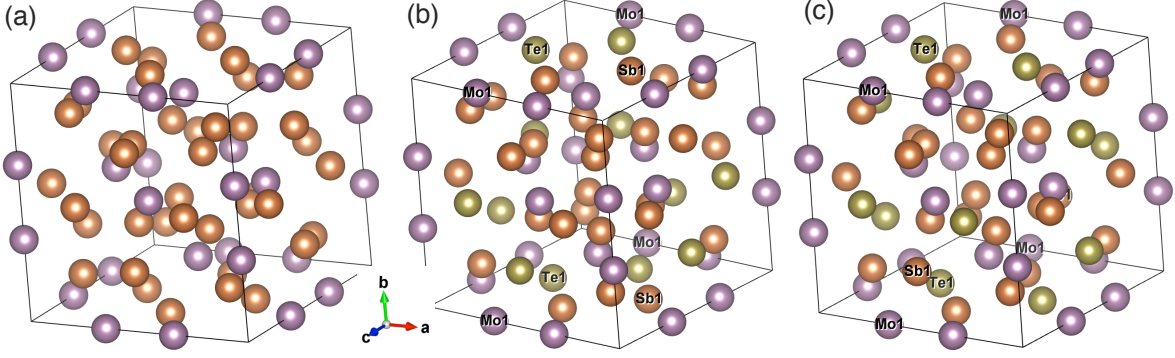Interestingly, by examining figure 7, one can observe

FIG. 2. Unitcell of a) Mo_3Sb_7, b) $Mo_3Sb_{5.5}Te_{1.5}$ Case1, and c) $Mo_3Sb_{5.5}Te_{1.5}$ Case2 (Mo atoms: purple color, Sb atoms: orange color, and Te atoms: light green color). Owing to strong site preference of Te atom in $Mo_3Sb_{7-x}Te_x$, only Sb(1) atoms at 12d site were replaced with Te atoms. Case1 and Case2 represent two possible Te doped configurations.

that the magnitude of phonon energy shifts upon Te doping is not uniform across the entire DOS. In particular, the phonon peak at ∼14 meV is most sensitive to doping ($\Delta E/E \sim 10\%$) while the peaks at ∼19 meV and ∼28 meV stiffen by about 5% and 6%, respectively. We identified the origin of this difference by determining which atomic sites are predominantly involved in these different frequency regions of the phonon DOS, based on our DFT simulations. As can be seen in figure 8, in the simulated partial phonon DOS, the modes at ∼14, 19, and 28 meV correspond predominantly to vibrations of Sb(12d), Sb(16f), and Mo(12e) atoms, respectively. Thus, the 14 meV peak is most sensitive to the Te doping, owing to the preferred Te substitution on the (12d) site. This behavior also reveals a larger bonding change around the Te dopants (12d), rather than an average renormalization of force-constants. We discuss this point in more details below.

B. Bonding

To investigate the modifications in chemical bonding responsible for the observed changes in vibrational properties, we first examine the electronic density of states (eDOS) of Mo_3Sb_7 and $Mo_3Sb_{5.5}Te_{1.5}$ obtained with DFT, shown in figure 9. As can be seen in this figure, the two doped supercells (case 1 and case 2) have a very similar eDOS, indicating that the particular location of Te dopants among 12d sites does not impact the results strongly. In both of the doped cells, the Fermi level (origin of energy axis) is pushed up towards the top of the valence band, compared to Mo_3Sb_7, with little distortion of the eDOS. This rigid band shift is rationalized as the filling of holes by the extra d electrons of Te. Because of the slope in the eDOS, this shift of E_F decreases the number of electronic states at the Fermi level ($\sim 42\%$), in agreement with previous observations by Candolfi *et al.* [16, 44] and

Xu *et al.* [15]. This decrease in eDOS at Fermi level originates from d-states of Mo(12e), and p-states of Sb(12d), Sb(16f), and Te(12d) atoms, with the projected eDOS showing suppressions at the Fermi level of about

$$\left\{ \left(N_{Mo(12e)}^{undoped}(E_F) - N_{Mo(12e)}^{doped}(E_F) \right) / N_{Mo(12e)}^{undoped}(E_F) \right\} \sim 18\%,$$

$$\left\{ \left(N_{Sb(12d)}^{undoped}(E_F) - N_{Sb(12d)}^{doped}(E_F) \right) / N_{Sb(12d)}^{undoped}(E_F) \right\} \sim 14\%,$$

$$\left\{ \left(N_{Sb(16f)}^{undoped}(E_F) - N_{Sb(16f)}^{doped}(E_F) \right) / N_{Sb(16f)}^{undoped}(E_F) \right\} \sim 18\%,$$

and $\left\{ \left(N_{Sb(12d)}^{undoped}(E_F) - N_{Te(12d)}^{doped}(E_F) \right) / N_{Sb(12d)}^{undoped}(E_F) \right\}$ $\sim 77\%$, respectively. In order to evaluate these changes, we have averaged the eDOS of supercells in case 1 and case 2.

In previous studies, some of us showed that sharp features in the eDOS near the Fermi level can result in a strong sensitivity of the electron-phonon coupling on either temperature or doping [47–50]. A similar behavior is observed in the present case of Mo_3Sb_7, with its strong sensitivity to band filling (Te doping). At low temperature, $Mo_3Sb_{5.3}Te_{1.7}$ follows the QH model, while the significantly larger electronic density at the Fermi level in Mo_3Sb_7 leads to a large deviations from QH behavior.

The change in density at the Fermi level impacts the effectiveness of screening of forces on the ion cores. Our first-principles lattice dynamics simulations of Mo_3Sb_7 and $Mo_3Sb_{5.5}Te_{1.5}$ illustrate this effect very clearly. As we can observe from figure 3, 4, and 8, our simulations capture the lattice dynamics of the two compositions very well, including the overall shape of the spectrum, as well as the frequencies of phonon peaks, and also the relative stiffening with Te doping. In particular, we observe the pronounced shift of the Te-dominated peak at ~ 18 meV in both simulations and measurements. A very good agreement is also achieved between our IXS measurements of phonon dispersions and our DFT simulations, as will be discussed below.

Given the reliability of our DFT simulations, we can rationalize the effects of Te doping observed experimentally by investigating the behavior of interatomic force-
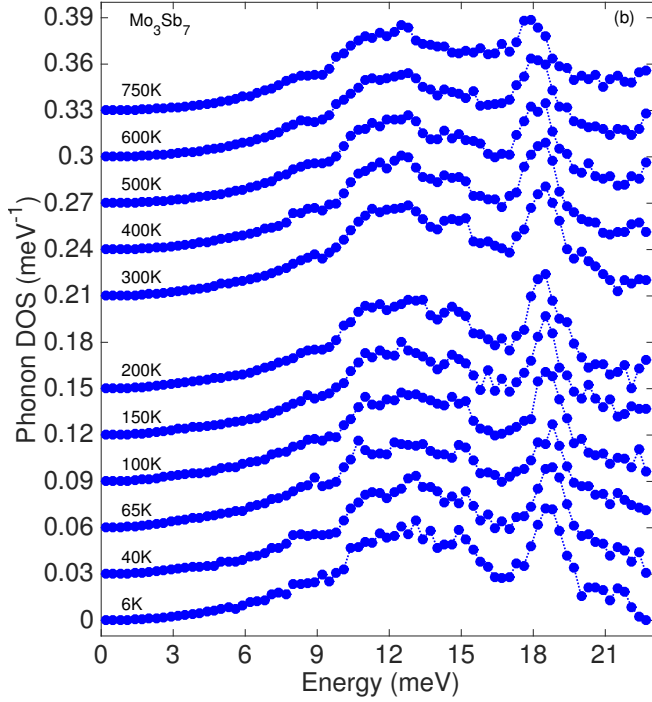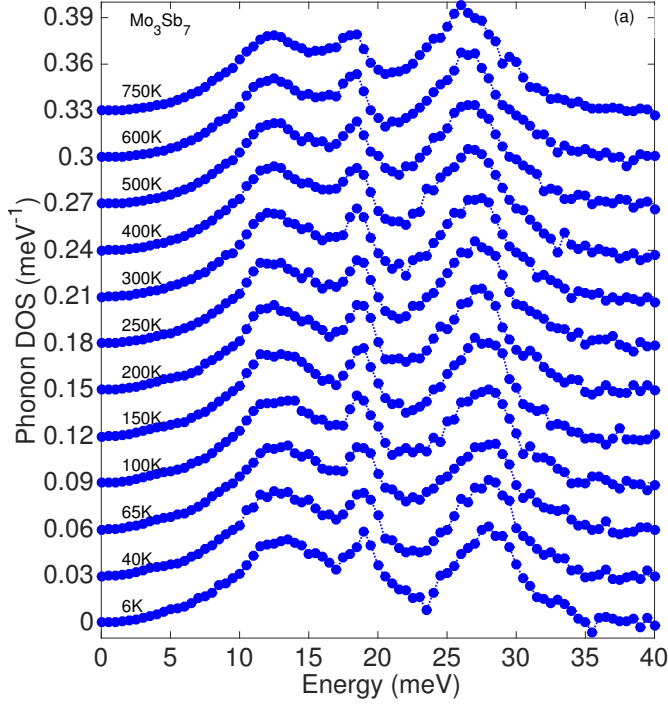
FIG. 3. Neutron-weighted phonon DOS of Mo$_3$Sb$_7$ measured with inelastic neutron scattering at different temperatures for incident neutron energies of a) 55 meV and b) 30 meV.

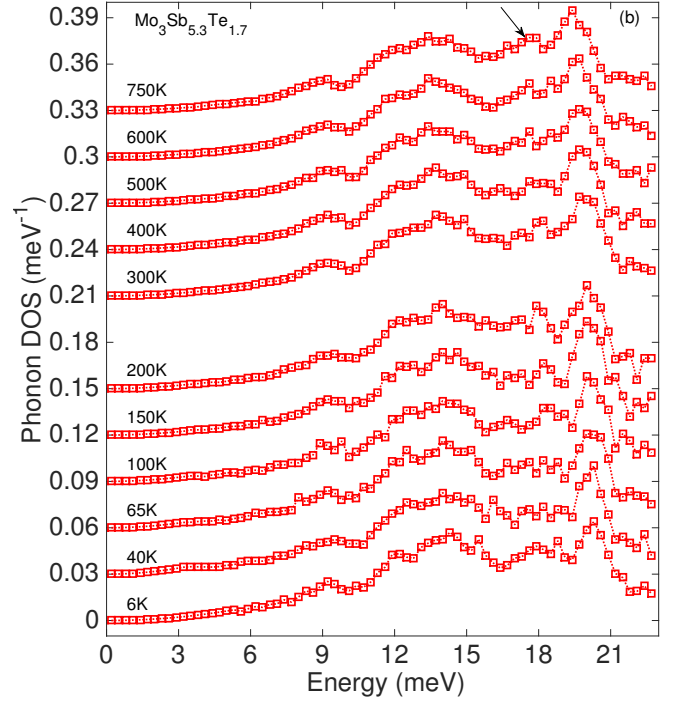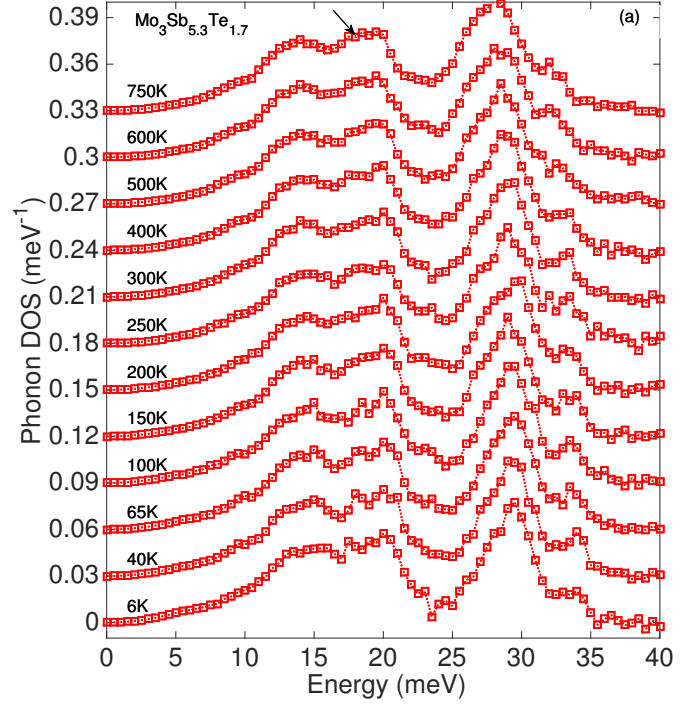FIG. 4. Neutron-weighted phonon DOS of Mo$_3$Sb$_{5.3}$Te$_{1.7}$ measured with inelastic neutron scattering at different temperatures for incident neutron energies of a) 55 meV and b) 30 meV. The peak denoted by arrow is described in text.
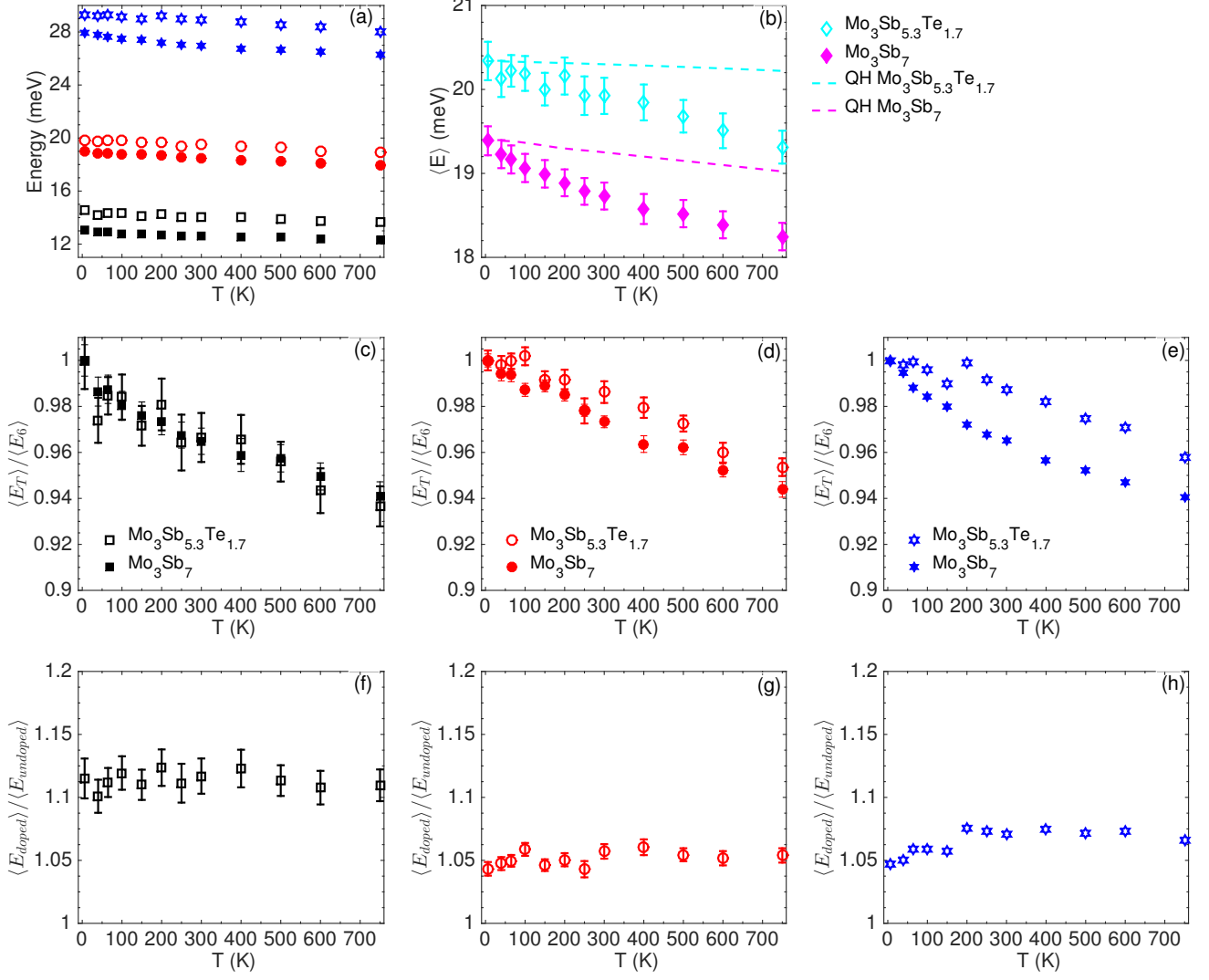
FIG. 5. a) Softening of phonon peaks at ∼14, 19, and 28 meV Mo$_3$Sb$_7$ (filled symbol) and Mo$_3$Sb$_{5.3}$Te$_{1.7}$ (empty symbol) measured from inelastic neutron scattering at different temperatures for incident neutron energies of 55 meV, b) Comparison of phonon mean energy $\langle E \rangle$ of Mo$_3$Sb$_7$ and Mo$_3$Sb$_{5.3}$Te$_{1.7}$. The dashed curves show the expected temperature dependence in the quasiharmonic model (QH), using the experimental data of thermal Gruneisen parameters and volumetric expansion. Moreover, the relative change in phonon peak energy c) ∼14 meV, d) ∼19 meV, and e) ∼28 meV with temperature $\langle E_T \rangle / \langle E_{6K} \rangle$, and doping $\langle E_{\mathrm{doped}} \rangle / \langle E_{\mathrm{undoped}} \rangle$ of phonon peaks at f) ∼14 meV, g) ∼19 meV, and h) ∼28 meV, respectively. In some panels, experimental error bars are comparable to the size of the symbols, and omitted.

constants. Table I lists the Born-von Karman (BvK) force constants of two compositions for first-nearest-neighbor (1NN) bonds between different pairs of atoms (see illustration in figure 10). The values reported in table I correspond to the L_1 norm of the 3×3 BvK force-constant matrix for each nearest pair of atoms. Since in the alloy supercell case 2, we replaced Sb with Te at 12d sites that are far apart, a direct comparison with 1NN force-constants is not possible. Thus, we limit ourselves to comparing case 1 with the undoped Mo$_3$Sb$_7$ cell. As can be seen in table I, the increase in force-

constants with Te doping is large, in particular for the bonds Mo(12e)-Mo(12e), Sb(12d)-Sb(12d), and Sb(16f)-Sb(16f). A slight decrease (∼ 6%) of the stiffness of the Mo(12e)-Sb(12d) 1NN bond is observed with Te doping. However, the Mo(12e)-Te(12d) bond is comparatively much stiffer, effectively stiffening the average Mo(12e)-Te/Sb(12d) bond in the alloy Mo$_3$Sb$_{5.5}$Te$_{1.5}$, in comparison to Mo(12e)-Sb(12d) in the pure compound Mo$_3$Sb$_7$. Accounting for the respective number of bonds in the alloy, we determine that the average Mo(12e)-Te/Sb(12d) bond stiffness increases by 108%, compared to the un-
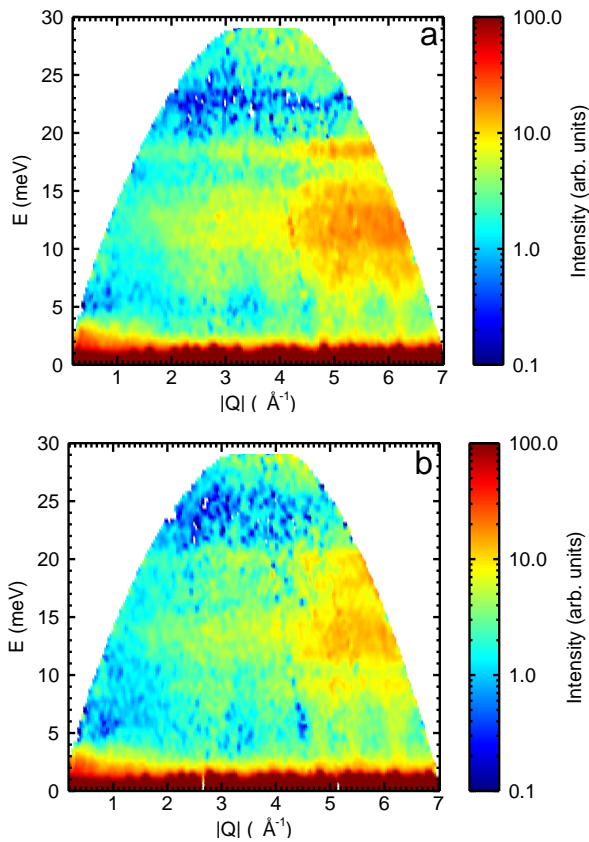
FIG. 6. Experimental scattering intensity function $S(\boldsymbol{Q}, E)$ of a) Mo_3Sb_7 and b) $Mo_3Sb_{5.3}Te_{1.7}$ measured with inelastic neutron scattering at 6 K for incident neutron energies of 30 meV. At low momentum transfers $|Q|$, we could not detect any magnetic scattering intensity in Mo_3Sb_7.

doped system. The large stiffening of this bond is reflected in the experimentally observed 10% stiffening of the ~ 14 meV phonon peak (figure 5), which is dominated by Sb/Te(12d) atomic motions, as seen in the partial phonon DOS (figure 8). Similarly, the $\sim 65\%$ stiffening of the bond stiffness for Mo(12e)-Mo(12e) and $\sim 45\%$ stiffening for Sb(16f)-Sb(16f) lead to the observed $\sim 6\%$ and $\sim 5\%$ stiffening of phonon peaks at ~ 28 and 19 meV, respectively. The change in local bonding upon Te substitution can also be seen by computing the stiffness of the local potential energy surface with DFT. Figure 11 shows the potential curves for small displacements of the Sb or Te atom from the 12d site, revealing a much stiffer bonding in the case of Te.

Based on the BvK force-constants, one can rationalize the behavior of experimental and computed phonon spectra. Considering the force-constants of Sb(12d)-Sb(12d) (2.23 eV/$Å^2$) and Te(12d)-Te(12d) (3.45 eV/$Å^2$) in doped cells, we observe that the pair of Te(12d) atoms is much stiffer than the Sb(12d) pair. This separates the frequencies of Te(12d)-dominated vibrations from Sb(12d) vibrations, giving rise to two distinct phonon

peaks at ~ 14 meV and ~ 18 meV. In contrast, the much smaller change in force-constants of Sb(12d)-Sb(16f) (1.91 eV/$Å^2$) and Te(12d)-Sb(16f) (2.01 eV/$Å^2$), and Sb(12d)-Mo(12e) (6.07 eV/$Å^2$) and Te(12d)-Mo(12e) (7.53 eV/$Å^2$) do not lead to any peak splitting (see figure 8).

C. Thermal Transport

In the remainder of the discussion, we focus on thermal transport properties. To quantify the impact of the change in bonding on the thermal conductivity, we consider the phonon dispersions for acoustic modes and low-energy optical branches. Figure 12 shows the phonon dispersions of Mo_3Sb_7 computed with DFT (thin lines), together with experimental momentum-resolved phonon energies from IXS measurements (markers), for both Mo_3Sb_7 and the Te-doped compound, at $T = 100$ K and 300 K. The phonon energies were determined from the IXS spectra at specific wave vectors, using the fitting procedure described in introduction and illustrated in Fig. 1. We find a very good agreement between the IXS measurements for Mo_3Sb_7 at 300 K and the DFT simulations (which used experimental lattice parameters at 300 K). Our DFT simulations for the phonon dispersions are in fair overall agreement with prior reports by Candolfi *et al.* [22] and Wiendlocha *et al.* [29, 31], except for the strong underestimation of the energy of the transverse acoustic branch along $\Gamma - N$ in these prior studies. This is likely the result of the smaller cells used to compute the phonons in these prior studies. The larger unit cells used in our computations were necessary to achieve the level of agreement with experiments observed here.

Considering the effect of Te alloying on phonon dispersions, we note that the amount of stiffening depends on the polarization of branches. The stiffening of transverse acoustic (TA) modes is pronounced along all directions measured (Γ–H, Γ–P, Γ–N). On the other hand, the LA mode stiffens noticeably with Te-doping along Γ–N, but there is little change of LA with doping, on average, along Γ–H. Tables II and III compare the phonon group velocities and elastic moduli derived from the phonon dispersions calculated with DFT and measured with IXS, as well as elastic moduli from resonant ultrasound measurements [51]. The elastic moduli from phonon group
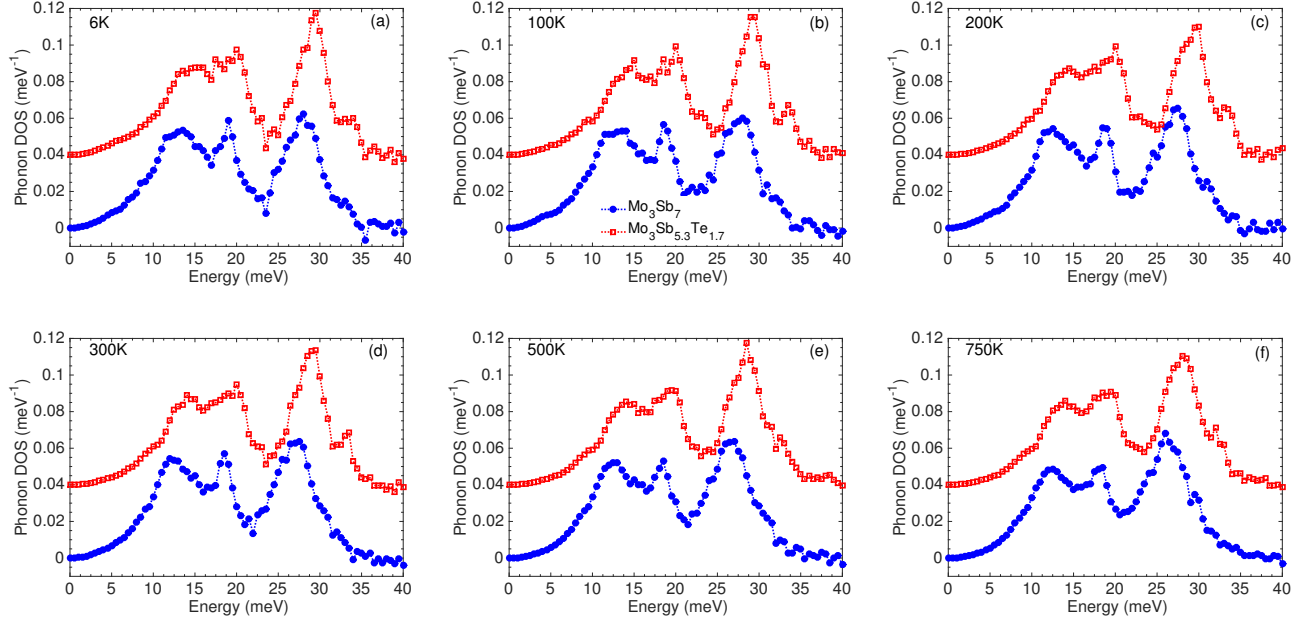
FIG. 7. Comparison of neutron-weighted phonon DOS of Mo_3Sb_7 (filled symbol) $Mo_3Sb_{5.3}Te_{1.7}$ (empty symbol) measured from inelastic neutron scattering at a) 6K, b) 100K, c) 200K, d) 300K, e) 500K, and f) 750K for incident neutron energy of 55 meV.
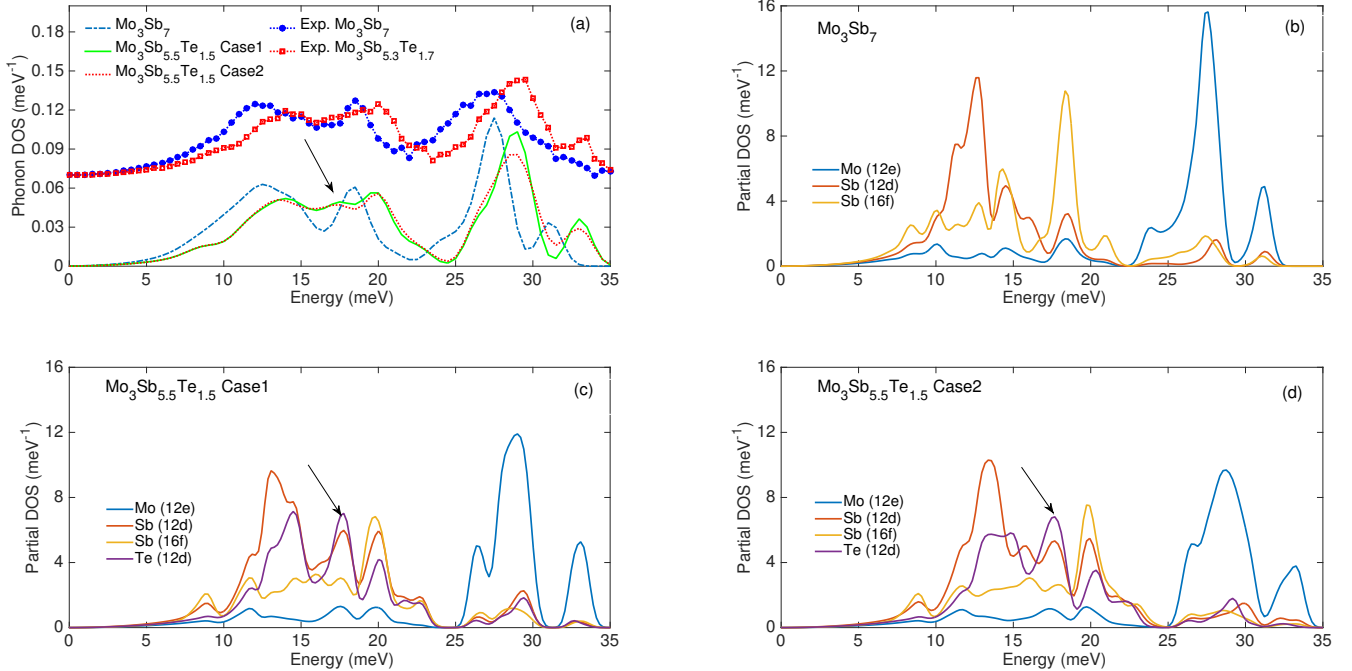

FIG. 8. a) DFT calculated neutron weighted phonon DOS convoluted with ARCS resolution function at 55 meV compared with experimental phonon measured at 300K, and b, c, d) partial phonon DOS of Mo_3Sb_7, $Mo_3Sb_{5.5}Te_{1.5}$ Case1, and $Mo_3Sb_{5.5}Te_{1.5}$ Case2, respectively, computed from first-principles. The peak denoted by an arrow corresponds to the Sb (12d) site, and is most sensitive to Te doping, as discussed in the text.
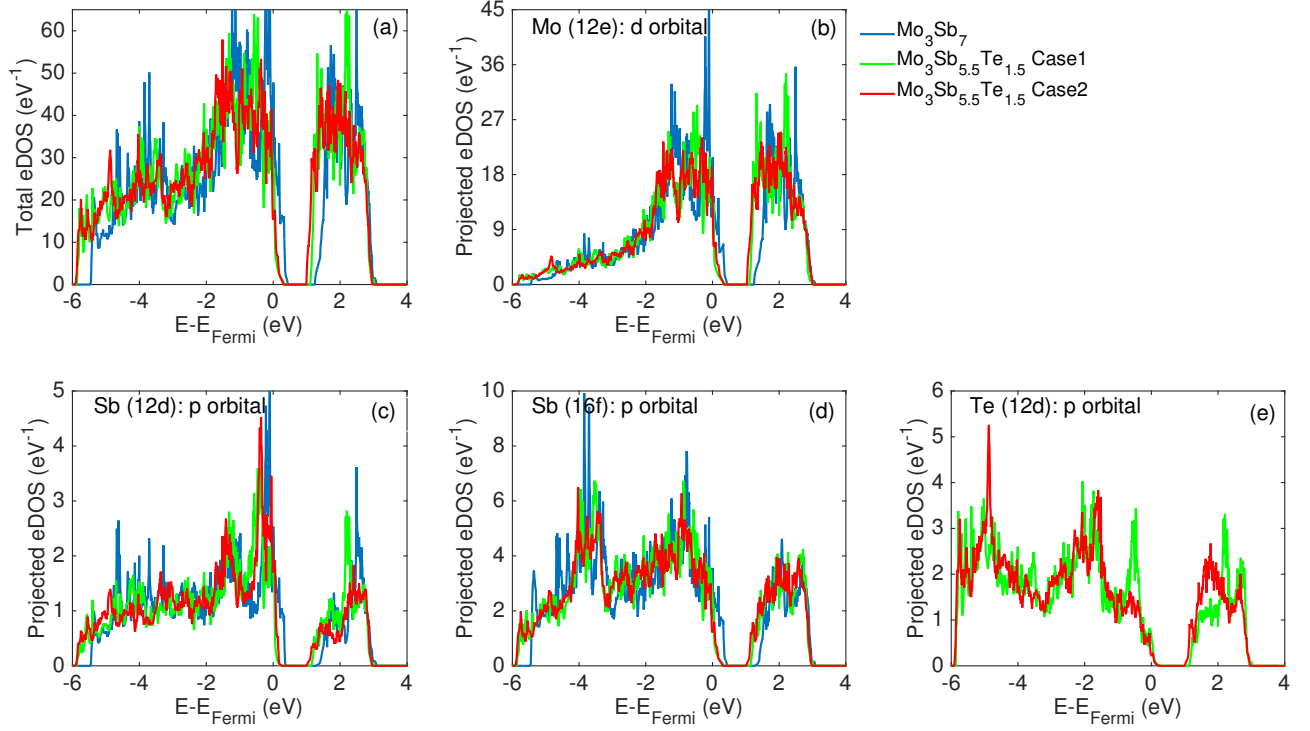
FIG. 9. Electronic density of states (eDOS) computed from first-principles for Mo_3Sb_7 and $Mo_3Sb_{5.5}Te_{1.5}$. (a) total eDOS. (b, c, d, e) site-projected eDOS.

TABLE I. Comparison of first-nearest-neighbor Born-von Karman (BvK) force-constants for Mo_3Sb_7 and $Mo_3Sb_{5.5}Te_{1.5}$. The values are L_1 norm of 3×3 BvK force-constant matrices (in eV/Å^2) between nearest pairs of atoms.

BvK FC (eV/Å^2)	$Mo_3Sb_{5.5}Te_{1.5}$	Mo_3Sb_7	% increase
Mo(12e)-Mo(12e)	6.16	3.76	63.70
Mo(12e)-Sb(12d)	6.07	6.45	-5.78
Mo(12e)-Sb(16f)	13.59	11.63	16.79
Mo(12e)-Te(12d)	7.53	⋯	⋯
Sb(12d)-Sb(12d)	2.23	1.37	62.60
Sb(12d)-Sb(16f)	1.91	1.63	17.48
Sb(12d)-Te(12d)	2.85	⋯	⋯
Sb(16f)-Sb(16f)	6.95	4.74	46.47
Sb(16f)-Te(12d)	2.01	⋯	⋯
Te(12d)-Te(12d)	3.45	⋯	⋯

velocity v_g have been calculated by solving $y = Hx$,

$$y = \begin{Bmatrix} \rho v_{g:[00\xi]LA}^2 \\ \rho v_{g:[00\xi]TA}^2 \\ 2\rho v_{g-[\xi\xi 0]LA}^2 \\ 2\rho v_{g-[\xi\xi 0]TA1}^2 \\ \rho v_{g-[\xi\xi 0]TA2}^2 \\ 3\rho v_{g-[\xi\xi\xi]TA}^2 \\ 2\rho v_{g-[\xi\xi\xi]LA}^2 \end{Bmatrix}; \quad H = \begin{bmatrix} 1 & 0 & 0 \\ 0 & 0 & 1 \\ 1 & 1 & 2 \\ 1 & -1 & 0 \\ 0 & 0 & 1 \\ 1 & -1 & 1 \\ 1 & 2 & 4 \end{bmatrix};$$

$$\text{and } x = \begin{Bmatrix} C_{11} \\ C_{12} \\ C_{44} \end{Bmatrix}. \quad (3)$$

where $\rho = 8640 \, kg/m^3$ is the density of Mo_3Sb_7 [52]. The density of Te-doped composition is assumed to be same as undoped composition, as Sb and Te have similar atomic masses ($m_{Te}/m_{Sb} \sim 1.05$), and lattice parameter are approximately equal (less than 0.1% different at 300K). The bulk modulus, $(C_{11} + 2C_{12})/3$, obtained from IXS dispersions is adiabatic K_{ad}, and can be converted to isothermal bulk modulus using $K_T = K_{ad}/(1+\alpha\gamma T)$. In all cases, we find that the change is practically negligible and within the experimental error bars, however (less than
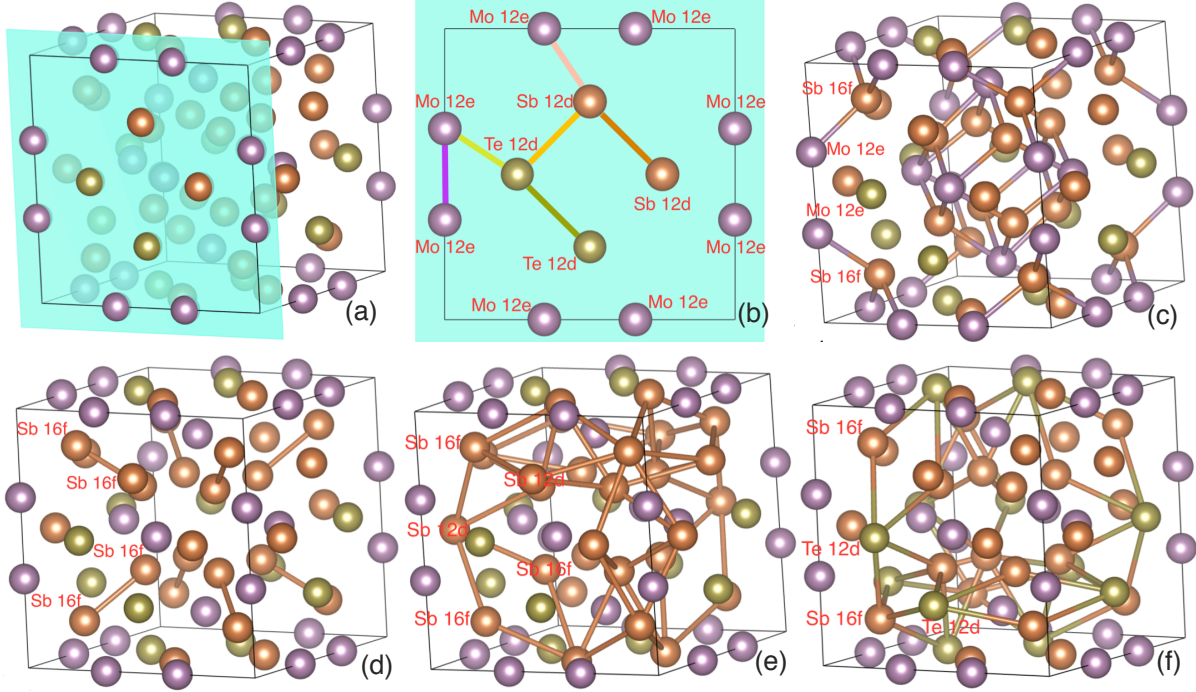
FIG. 10. First-nearest-neighbor interatomic bonds between the different pairs of atoms considered in table I and in the text. a) and b) Mo(12e)-Mo(12e) , Mo(12e)-Sb(12d), Mo(12e)-Te(12d), Sb(12d)-Sb(12d) , Sb(12d)-Te(12d), and Te(12d)-Te(12d), c) Mo(12e)-Sb(16f), d) Sb(16f)-Sb(16f), e) Sb(12d)-Sb(16f), and f) Sb(16f)-Te(12d).
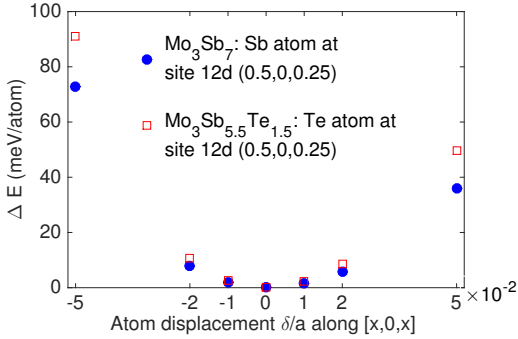

FIG. 11. Comparison of change in DFT electronic energy of Mo_3Sb_7 (filled symbol) and $Mo_3Sb_{5.5}Te_{1.5}$ (empty symbol) while displacing Sb/Te atom at site 12d along [x,0,x], by a relative amount δ/a. Here, a is the lattice constant of Mo_3Sb_7 and $Mo_3Sb_{5.5}Te_{1.5}$ at 300 K.

0.075%). The good agreement between experimental IXS data, resonant ultrasonic measurements, and DFT simulations provides confidence in our methods and results. We note that our experimental ($K_T = 112 \pm 18$ GPa) and computational results ($K_T = 134$ GPa) for the bulk modulus are much larger than the estimates ($K_T = 72$–73.6 GPa) reported by Candolfi et al. [22]

Using the phonon group velocities determined from DFT (validated against IXS), we proceed to estimate the phonon relaxation times and phonon mean free paths for the two compositions. In this analysis, we use the $\boldsymbol{q}$-dependent phonon group velocity $v_g(\boldsymbol{q})$ of acoustic modes obtained from DFT simulations, for both the parent Mo_3Sb_7 and doped $Mo_3Sb_{5.5}Te_{1.5}$. First, we estimate an average relaxation time $\overline{\tau}$ and average mean-free-path $\overline{\Lambda}$ on a $41 \times 41 \times 41$ $\boldsymbol{q}$−point mesh, using the expression for the lattice thermal conductivity in the relaxation time approximation, $\overline{\tau} = \frac{1}{3}\overline{C_v v_g^2(\boldsymbol{q})}/\kappa_L$ and $\overline{\Lambda} = \frac{1}{3}\overline{C_v v_g(\boldsymbol{q})}/\kappa_L$, and κ_L from values reported by Candolfi et al. [16]. Results are reported in table IV. From these results, we can observe that the average phonon relaxation time and average mean-free-path both show a clear increase upon Te doping, especially at T=100K. The decrease in phonon linewidth Γ_{LW} at 300K, which is inversely proportional to the phonon relaxation time $\tau = 1/2\Gamma_{LW}$, is also observed in our experimental IXS data, as can be seen in figure 1. We note that the relaxation times, τ, in figure 1 are for relatively high-energy phonon modes and are thus substantially larger than the average values in table IV. This is due to the strong increase of scattering rates with phonon frequency, between ω^2 and ω^4 (see Eq. (4)). In addition, the modes in figure 1 are in the band of low-energy optic modes, opening additional phonon-phonon scattering channels. The low-energy acoustic phonons, which are primary heat carriers, are resolution limited in our IXS measurements. Our
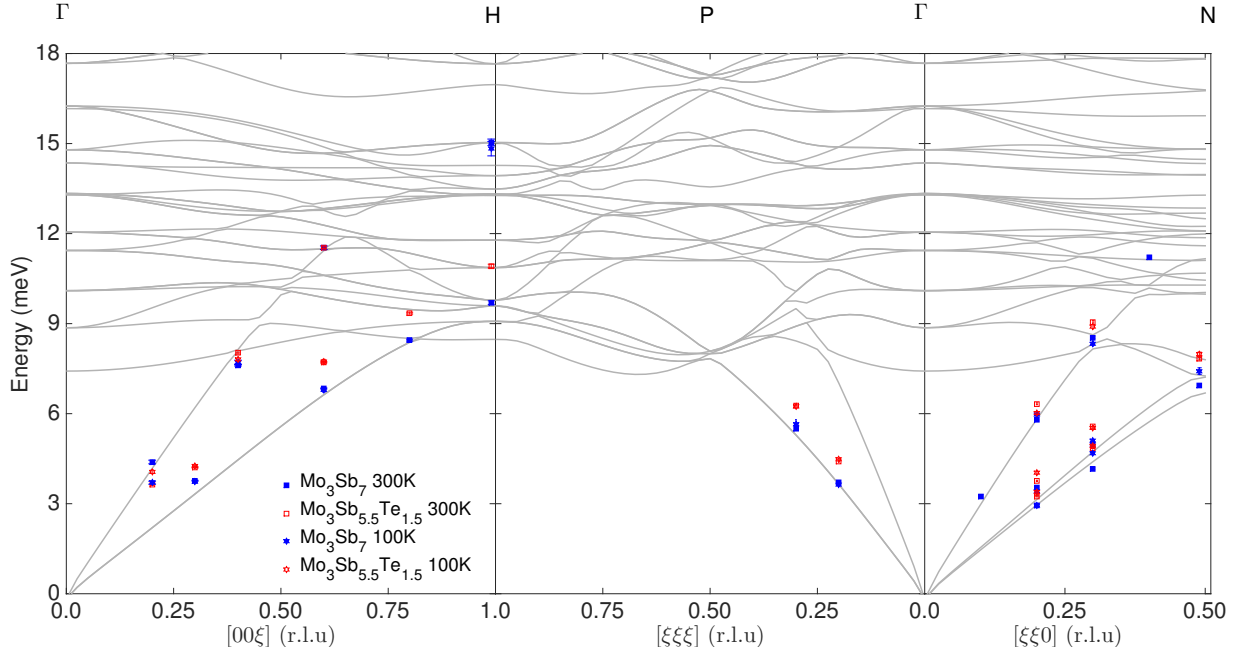
FIG. 12. Phonon energies of Mo_3Sb_7 (filled symbol) and $Mo_3Sb_{5.5}Te_{1.5}$ (empty symbol) obtained from experimental inelastic x-ray scattering measurements. The light-gray lines are DFT simulations of phonon dispersions for Mo_3Sb_7 along high symmetry directions, which can be compared with the filled blue squares for IXS data (Mo_3Sb_7 at 300 K).

TABLE II. Phonon group velocities (v_g in m/s) of long-wavelength acoustic phonons for Mo_3Sb_7 and $Mo_3Sb_{5.5}Te_{1.5}$, calculated from DFT and measured with IXS. Phonon group velocities from IXS data has been estimated by fitting linear function to two q−points along that particular direction with constraint – phonon energy is zero at Γ point.

Direction	Mode	Mo_3Sb_7 v_g (m/s)			$Mo_3Sb_{5.5}Te_{1.5}$ v_g (m/s)			
		DFT	Exp. 100K	Exp. 300K	Case1 DFT	Case2 DFT	Exp. 100K	Exp. 300K
Γ − H	TA	2578	2626±157	2650±152	3153	3180	2979±176	2975±156
	LA	4857	4461±103	4408±386	4830	4380	4515±110	4636±254
Γ − N	TA1	2483	2538±107	2292±91	2228	2589	2704±59	2650±6
	TA2	2609	2779±10	2736±132	3211	3193	3049±213	3046±24
	LA	4929	4596±242	4737±335	5280	5334	4862±59	4972±177
Γ − P	TA	2501	2500±64	2455±26	2471	2821	2806±154	2816±111
	LA	4923	⋯	⋯	5497	5409	⋯	⋯

measurements of phonon linewidths at T=100K for the Te-doped sample are limited by the experimental resolution, and doping effects cannot be quantified at this temperature. An upper-bound estimate for the maximum phonon linewidth in the Te-doped sample at 100 K is 0.9 ± 0.2 meV along [0 K 0] for K = 0.2 r.l.u. Moreover, the 20% to 45% change in experimental Γ_{LW} or τ with Te doping along the measured high symmetry directions at 300K is in generally good agreement with our estimate of the change in average relaxation time in table IV, i.e., $\{\tau_{\text{doped}}^{300\,\text{K}} - \tau_{\text{undoped}}^{300\,\text{K}}\}/\tau_{\text{undoped}}^{300\,\text{K}} = 0.41$. From the data in tables II, III, and IV, we can assess the respective contributions of the group velocities and lifetimes to the Te-induced increase in κ_L. We find that at 100 K, the larger phonon group velocities in the Te-doped material accounts for just ∼25% of the increase in κ_L, while the main effect is due to the increase in phonon relaxation

times. However, at 300 K the stiffening of phonon group velocities upon doping accounts for ∼70% of the increase in κ_L (this figure assumes that the doping-induced stiffening is independent of temperature, which is well justified in view of Fig. 5-f,g,h). This can be understood as a larger effect of electron-phonon scattering on the phonon relaxation times at low temperature, leading to the large suppression in κ_L at 100 K, as discussed more quantitatively below.

Several scattering mechanisms contribute to the overall phonon scattering rates, τ^{-1}, which, following Matthiessen's rule, can be summed if assumed to be independent processes. In the present analysis, we consider boundary scattering (τ_B^{-1}), point-defect scattering (τ_{PD}^{-1}), umklapp scattering from phonon anharmonicity

TABLE III. Comparison of elastic moduli C_{11}, C_{12}, C_{44}, and iso-thermal bulk modulus K_T calculated from DFT and derived from slopes of IXS dispersions, for Mo_3Sb_7 and $Mo_3Sb_{5.5}Te_{1.5}$. For the Te-doped system, the DFT results are averaged over Case1 and Case2.

Modulus	Mo_3Sb_7					$Mo_3Sb_{5.5}Te_{1.5}$		
	DFT	Exp. 100K	Ref. [51] 100K	Exp. 300K	Ref. [51] 300K	DFT	Exp. 100K	Exp. 300K
C11 (GPa)	204	173±28	161	172±28	178	195	183±22	191±27
C12 (GPa)	98	68±11	90	83±13	87	103	60±7	70±10
C44 (GPa)	57	61±10	72	65±10	68	92	82±10	82±11
K_T (GPa)	134	103±16	114	112±18	117	133	100±12	110±15

TABLE IV. Average phonon relaxation time (τ) and average mean-free-path (Λ) of three lowest phonon branches calculated from expression of lattice thermal conductivity $\kappa_L = \frac{1}{3}\overline{C_v v_g^2(\boldsymbol{q})}\tau = \frac{1}{3}\overline{C_v v_g(\boldsymbol{q})}\Lambda$, where group velocity at given $\boldsymbol{q}$, $v_g(\boldsymbol{q})$, and specific heat capacity at constant volume, C_v, have been obtained from DFT simulations for Mo_3Sb_7 and $Mo_3Sb_{5.5}Te_{1.5}$ at T = 300K and 100K. The lattice thermal conductivity (κ_L) values are taken from Ref. [16]

	Mo_3Sb_7		$Mo_3Sb_{5.5}Te_{1.5}$			
			Case1		Case2	
T in Kelvin	100	300	100	300	100	300
Average relaxation time (τ) in ps	10.3	18.3	40.2	25.3	41.7	26.2
Average mean-free-path (Λ) in Å	228	401	1160	727	1190	746

(τ_U^{-1}), and electron-phonon scattering (τ_{ep}^{-1}):

$$\tau^{-1} = \tau_B^{-1} + \tau_{PD}^{-1} + \tau_U^{-1} + \tau_{ep}^{-1}. \quad (4)$$

$$\tau^{-1} = \frac{v_g}{L} + 3V\frac{\omega^4}{\pi v_g^3}S^2$$
$$+ P\frac{\hbar\gamma^2}{Mv_g^2\theta_D}\omega^2 T^n \exp\left(-\frac{\theta_D}{mT}\right) + C_{ep}\frac{\omega^2}{v_g^2}, \quad (5)$$

where L is the grain size, V is the volume per unit cell, θ_D is the Debye temperature, ω is the phonon frequency, γ is an average Grüneisen parameter, and P, n, and m are umklapp scattering parameters of order one. Scattering by point-defects, S, is estimated as a combination of three terms – perturbations in mass, force-constant, and nearest-neighbor distance. The expression of S^2 and C_{ep} are given by:[20, 21]

$$S^2 = S_1^2 + (S_2 + S_3)^2,$$
$$S_1 = \frac{1}{\sqrt{12}}\left(\frac{\Delta M}{M}\right),$$
$$S_2 = \frac{1}{\sqrt{6}}\left(\frac{\Delta f}{f}\right),$$
$$S_3 = \sqrt{24}\left(\frac{\Delta R}{R}\right), \text{ and}$$
$$C_{ep} = \frac{4\rho m^* v_F L_e}{15d}. \quad (6)$$

Here, ΔM, Δf, and ΔR are the perturbation in mass, force-constants, and nearest-neighbor distances, ρ is the electron concentration, m^* is the effective mass of electrons, v_F is the Fermi velocity, L_e is the mean free path of electrons, and d is the mass density. The change in nearest neighbor distance (or local distortions) with Te doping is less than 0.1%, and is not considered in this analysis as it is much smaller than the perturbations in mass

and force-constants. Debye temperatures $\theta_D = 282\,\text{K}$ for Mo_3Sb_7 and $\theta_D = 326\,\text{K}$ for $Mo_3Sb_{5.4}Te_{1.6}$ were estimated by Shi *et al.* from their heat capacity measurements [13]. We have calculated the Debye temperature from the first moment of the measured phonon spectrum $g(E)$, as $\theta_D = \frac{4\langle E\rangle}{3k_B}$, where $\langle E\rangle = \int g(E)E\,dE$ and k_B is Boltzmann's constant. For Mo_3Sb_7, we estimate Debye temperatures of $295 \pm 3\,\text{K}$ and $290 \pm 3\,\text{K}$ at $100\,\text{K}$ and $300\,\text{K}$, respectively. Similarly, for $Mo_3Sb_{5.5}Te_{1.5}$ we estimate $\theta_D = 312 \pm 4\,\text{K}$ and $308 \pm 4\,\text{K}$ at $100\,\text{K}$ and $300\,\text{K}$, respectively. We used the reported value of grain size ($\sim 100\,\mu m$) in thermal conductivity measurements [16, 19], to estimate L for boundary scattering. The parameters P, n, and m have been kept constant at 1.0, 1.25, and 3.0, respectively, for both compositions. For Mo_3Sb_7, we do not include any mass or force-constant disorder ($S = 0$), while for $Mo_3Sb_{5.5}Te_{1.5}$, the electron-phonon coupling constant C_{ep} is set to zero (justified based on the much smaller carrier concentration). Based on mass and force-constant perturbations with Te doping (see table I), the terms S_1 and S_2 are 3.70×10^{-3} and 4.06×10^{-2}, respectively. Based on κ_L values reported by Candolfi *et al.* [16, 19], the value of C_{ep} for Mo_3Sb_7 was estimated to be 1.00×10^{-8} m^2/sec. The $\boldsymbol{q}$- and branch-dependent phonon frequencies and group velocities in all of our lattice thermal conductivity calculations are determined from DFT simulations as described earlier.

The resulting lattice thermal conductivities $\kappa_L(T)$ for the pure and doped systems are shown in figure 13-a,b, respectively. Our results for the doped composition at all temperatures are in fair agreement with values of κ_L reported by Candolfi *et al.* [16, 19]. As can be observed, in $Mo_3Sb_{5.5}Te_{1.5}$ the magnitude and temperature of the peak in κ_L is controlled by point-defect scattering processes at low temperatures, and at high temperatures Umklapp processes become large and determine the slope of lattice thermal conductivity. The dominance of Umk-
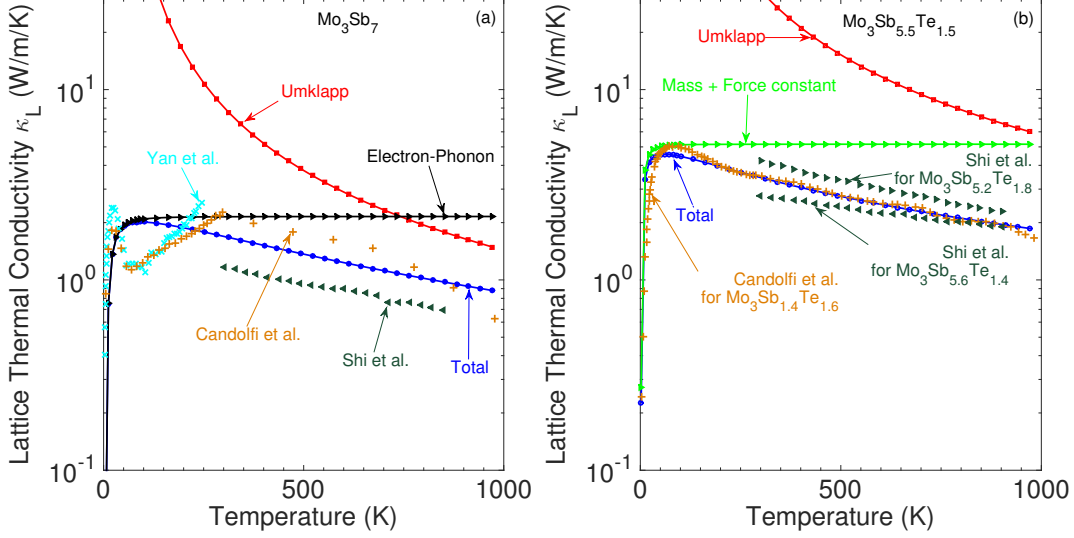
FIG. 13. Model of the lattice thermal conductivity κ_L of a) Mo_3Sb_7 and b) $Mo_3Sb_{5.5}Te_{1.5}$, considering several phonon scattering processes, as described in the text. '×' (cyan color), '◁' or '▷' (dark green), and '+' (brown color) are lattice thermal conductivity data from Yan *et al.* [27], Shi *et al.* [13], and Candolfi *et al.* [16, 19], respectively. In b) '+' (brown color), '◁' (dark green), and '▷' (dark green) data points are for $Mo_3Sb_{5.4}Te_{1.6}$, $Mo_3Sb_{5.6}Te_{1.4}$, and $Mo_3Sb_{5.2}Te_{1.8}$ composition.

lapp scattering at high temperature is consistent with the analysis of κ_L by Shi et al. [13]. However, the prior study by Shi et al. [13] underestimated the point-defect scattering by only considering the contribution from mass perturbation and ignoring the effect of force constant perturbation in $Mo_3Sb_{5.5}Te_{1.5}$. However, according to our estimates, the force-constant perturbation ($S_2 = 4.06 \times 10^{-2}$) is approximately ten times greater than the mass perturbation ($S_1 = 3.70 \times 10^{-3}$), and cannot be ignored.

The very low lattice thermal conductivity in Mo_3Sb_7 is a result of strong electron-phonon coupling in this compound, combined with the large unit cell leading to many flat optical branches. From figure 13(a), we can observe that κ_L is greatly suppressed by scattering processes from electron-phonon interaction at low temperature, which still contribute significantly at room temperature. As described earlier, the electron-phonon interaction affects both the phonon group velocities and the relaxation times. From our calculations, we find that in Mo_3Sb_7 at 100K, the suppression in the phonon relaxation time compared to $Mo_3Sb_{5.5}Te_{1.5}$ is dominated by the electron-phonon scattering, i.e., $\tau^{-1} \approx \tau_{ep}^{-1}$. Moreover, at 300K, electron-phonon scattering contributes about 85% of the total phonon scattering rate compatible with large electron-phonon coupling in metals [53], while the increase in Umklapp scattering accounts for most of the rest. We note that we have ignored the interaction of phonons with Mo-Mo magnetic dimers and local distortions at low temperature, where magnetic properties may influence the thermal transport behavior. Consequently, our model does not capture the minimum in κ_L at ~ 55 K reported by Candolfi *et al.* [16] and Yan *et*

al. [27]. We attempted to include this extra source of phonon scattering with a resonance-scattering term [54], but the pronounced dip in experimental curves could not be reproduced. It is likely that the unusual κ_L of Mo_3Sb_7 near ~ 55 K is closely related to its structural instability induced by the competing magnetic interactions [32], but a more complex phonon scattering model, beyond the scope of the present study, would be required to describe this effect. To summarize the present discussion, we emphasize that at temperatures ($200 \leqslant T \leqslant 750K$), the increase in κ_L with Te doping is primarily arising from the reduction in electron-phonon coupling, which significant increases the phonon group velocities and relaxation times.

VI. CONCLUSION

We have investigated phonons in the candidate thermoelectric material $Mo_3Sb_{7-x}Te_x$, using inelastic neutron and x-ray scattering, as well as DFT simulations. The phonon DOS exhibits a strong overall stiffening upon alloying with Te, which is well reproduced in our DFT simulations of alloy supercells. We also observed that the phonon DOS for both Mo_3Sb_7 and $Mo_3Sb_{5.3}Te_{1.7}$ shows a significant softening with increasing temperature, beyond the effect of thermal expansion in the quasi-harmonic approximation. Our first-principles phonon simulations for $Mo_3Sb_{7-x}Te_x$ reveal that Te doping leads to strong local perturbations of the bonding environment and interatomic force-constants. In particular, the bonds Sb(12d)-Sb/Te(12d), Mo(12e)-Mo(12e), and

Sb(16f)-Sb(16f) stiffen by as much as ∼108%, 65%, and 45%, respectively, upon substitution of Te at the Sb(12d) site. As a result of this strong local perturbation, the phonon spectrum stiffens in a non-uniform manner. Furthermore, our phonon dispersion measurements with IXS, combined with DFT simulations, reveal that the suppression in electron-phonon coupling upon Te-doping largely accounts for the increase in lattice thermal conductivity. This suppressed electron-phonon coupling increases the phonon group velocities and phonon relaxation times, despite the introduction of significant impurity scattering from force-constant disorder.

VII. ACKNOWLEDGEMENTS

[1] G. Snyder and E. Toberer, Nature Materials **7**, 105 (2008).

[2] A. Minnich, M. Dresselhaus, Z. Ren, and G. Chen, Energy Environmental Science **2**, 466 (2009).

[3] K. Biswas, J. He, I. Blum, C.-I. Wu, T. Hogan, D. Seidman, V. Dravid, and M. Kanatzidis, Nature **489**, 414 (2012).

[4] V. Keppens, D. Mandrus, B. Sales, B. Chakoumakos, P. Dai, R. Coldea, M. Maple, D. Gajewski, E. Freeman, and S. Bennington, Nature **395**, 876 (1998).

[5] O. Delaire, J. Ma, K. Marty, A. May, M. McGuire, M.-H. Du, D. Singh, A. Podlesnyak, G. Ehlers, M. Lumsden, and B. Sales, Nature Materials **8**, 614 (2011).

[6] M. Nielsen, V. Ozolins, and J. Heremans, Energy Environmental Science **6**, 570 (2013).

[7] B. Poudel, Q. Hao, Y. Ma, Y. Lan, A. Minnich, B. Yu, X. Yan, D. Wang, A. Muto, D. Vashaee, X. Chen, J. Liu, M. Dresselhaus, G. Chen, and Z. Ren, Science **320**, 634 (2008).

[8] M. Koza, M. Johnson, R. Viennois, H. Mutka, L. Girard, and D. Ravot, Nature Materials **7**, 805 (2008).

[9] M. Christensen, A. Abrahamsen, N. Christensen, F. Juranyi, N. Andersen, K. Lefmann, J. Andreasson, C. Bahl, and B. Iversen, Nature Materials **7**, 811 (2008).

[10] J. Ma, O. Delaire, A. May, C. Carlton, M. McGuire, L. VanBebber, D. Abernathy, G. Ehlers, T. Hong, A. Huq, W. Tian, V. Keppens, Y. Y. Shao-Horn, and B. Sales, Nature Nanotechnology **8**, 445 (2013).

[11] D. Voneshen, K. Refson, E. Borissenko, M. Krisch, A. Bosak, A. Piovano, E. Cemal, M. Enderle, M. Gutmann, M. Hoesch, M. Roger, L. Gannon, A. Boothroyd, S. Uthayakumar, D. Porter, and J. Goff, Nature Materials **12**, 1028 (2013).

[12] J.-S. Rhyee, K.-H. Lee, S.-M. Lee, E. Cho, S.-I. Kim, E. Lee, Y. Kwon, J. Shim, and G. Kotliar, Nature **459**, 965 (2009).

[13] X. Shi, Y. Pei, G. Snyder, and L. Chen, Energy & Environmental Science **4**, 4086 (2011).

[14] D. Parker, M.-H. Du, and D. Singh, Physical Review B **83**, 245111 (2011).

[15] H. Xu, K. Kleinke, T. Holgate, H. Zhang, Z. Su, T. Tritt, and H. Kleinke, Journal of Applied Physics **105**, 053703 (2009).

[16] C. Candolfi, B. Lenoir, A. Dauscher, J. Hejtmanek, and J. Tobola, Physical Review B **79**, 235108 (2009).

[17] C. Candolfi, B. Lenoir, A. Dauscher, E. Guilmeau, J. Hejtmanek, J. Tobola, B. Wiendlocha, and S. Kaprzyk, Physical Review B **79**, 035114 (2009).

[18] C. Candolfi, B. Lenoir, J. Leszczynski, A. Dauscher, and E. Guilmeau, Journal of Applied Physics **105**, 083701 (2009).

[19] C. Candolfi, B. Lenoir, C. Chubilleau, A. Dauscher, and E. Guilmeau, Journal of Physics: Condensed Matter **22**, 025801 (2010).

[20] P. Klemens, *Solid State Physics: Advances in Research and Applications – Thermal Conductivity and Lattice Vibrational Modes* (Vol. 7, Academic Press Inc., New York, 1958).

[21] T. Tritt, *Thermal Conductivity: Theory, Properties, and Applications* (Kluwer Academic/Plenum Publishers, New York, 2004).

[22] C. Candolfi, B. Lenoir, A. Dauscher, M. Koza, M. de Boissieu, M. Sternik, and K. Parlinski, Physical Review B **84**, 224306 (2011).

[23] Z. Bukowski, D. Badurski, J. Stepien-Damm, and R. Troc, Solid State Communications **123**, 283 (2002).

[24] T. Koyama, H. Yamashita, Y. Takahashi, T. Kohara, I. Watanabe, Y. Tabata, and H. Nakamura, Physical Review Letters **101**, 126404 (2008).

[25] T. Koyama, H. Yamashita, T. Kohara, Y. Tabata, and H. Nakamura, Materials Research Bulletin **44**, 1132 (2009).

[26] V. Tran, W. Miiller, and Z. Bukowski, Physical Review Letters **100**, 137004 (2008).

[27] J.-Q. Yan, M. McGuire, A. May, H. Cao, A. Christianson, D. Mandrus, and B. Sales, Physical Review B **87**, 104515 (2013).

[28] C. Candolfi, B. Lenoir, A. Dauscher, C. Bellouard, J. Hejtmanek, E. Santava, and J. Tobola, Physical Review Letters **99**, 037006 (2007).

[29] B. Wiendlocha, J. Tobola, M. Sternik, S. Kaprzyk, K. Parlinski, and A. Oles, Physical Review B **78**, 060507 (2008).

[30] H. Okabe, S. Yano, T. Muranaka, , and J. Akimitsu, Journal of Physics: Conference Series **150**, 052196 (2009).

[31] B. Wiendlocha and M. Sternik, Intermetallics **53**, 150 (2014).

[32] J.-Q. Yan, M. McGuire, A. May, D. Parker, D. Mandrus, and B. Sales, Physical Review B **92**, 064507 (2015).

[33] M. Stone, J. Niedziela, D. Abernathy, L. DeBeer-Schmitt, G. Ehlers, O. Garlea, G. Granroth, M. Graves-Brook, A. Kolesnikov, A. Podlesnyak, and B. Winn, Review of Scientific Instruments **85**, 045113 (2014).

[34] MANTID, "http://www.mantidproject.org," (2015).

[35] B. Fultz, T. Kelley, M. Mckerns, J. Lee, O. Delaire, and M. Kresch, *Experimental Inelastic Neutron Scattering: Introduction to DANSE* (2011).

[36] T. Toellner, A. Alatas, and A. Said, Journal of Synchrotron Radiation **18**, 605 (2011).

[37] A. Said, H. Sinn, and R. Divan, Journal of Synchrotron Radiation **18**, 492 (2011).

[38] S. Lovesey, *Theory of neutron scattering from condensed matter* (Clarendon Press, Oxford, 1984).

[39] VASP, "Vienna ab initio simulation package: http://www.vasp.at/," (2015).

[40] G. Kresse and J. Hafner, Physical Review B **47**, 558 (1993).

[41] G. Kresse and J. Furthmüller, Physical Review B **54**, 11169 (1996).

[42] G. Kresse and J. Furthmüller, Computational Materials Science **6**, 15 (1996).

[43] J. Perdew, K. Burke, and M. Ernzerhof, Physical Review Letters **77**, 3865 (1996).

[44] C. Candolfi, B. Lenoir, A. Dauscher, J. Tobola, S. Clarke, and R. Smith, Chemistry of Materials **20**, 6556 (2008).

[45] A. Togo, "Phonopy user's manual: http://phonopy.sourceforge.net/," (2015).

[46] A. A. Togo, F. Oba, and I. Tanaka, Physical Review B **78**, 134106 (2008).

[47] O. Delaire, M. S. Lucas, J. A. Muñoz, M. Kresch, and B. Fultz, Physical Review Letters **101**, 105504 (2008).

[48] O. Delaire, M. Kresch, J. A. Muñoz, M. S. Lucas, J. Y. Y. Lin, and B. Fultz, Physical Review B **77**, 214112 (2008).

[49] O. Delaire, A. F. May, M. A. McGuire, W. D. Porter, M. S. Lucas, M. B. Stone, D. L. Abernathy, V. Ravi, S. A. Firdosy, and G. J. Snyder, Physical Review B **80**, 184302 (2009).

[50] O. Delaire, K. Marty, M. Stone, P. Kent, M. Lucas, D. Abernathy, D. Mandrus, and B. Sales, Proceedings of the National Academy of Sciences **108**, 4725 (2011).

[51] L. Vanbebber, *Synthesis, Basic Characterization, and Resonant Ultrasound Studies of Novel Materials: Iron-based Superconductors and Mo_3Sb_7-based Thermo-electrics*, Ph.D. thesis, University of Tennessee, Knoxville (2013).

[52] P. Villars, "Material Phases Data System: http://materials.springer.com/isp/crystallographic /docs/sd_1125052," (2015).

[53] G. Grimvall, *The electron-phonon interaction in metals* (North-Holland Pub. Co., U.S.A., 1981).

[54] R. Pohl, Physical Review Letters **8**, 481 (1962).